Available online at www.sciencedirect.com
ScienceDirect
International Journal of Heat and Mass Transfer 51 (2008) 155–168
International Journal of HEAT and MASS TRANSFER
www.elsevier.com/locate/ijhmt

# Sharp interface numerical simulation of directional solidification of binary alloy in the presence of a ceramic particle

Yi Yang, J.W. Garvin, H.S. Udaykumar *

*Department of Mechanical and Industrial Engineering, University of Iowa, Iowa City, IA-52242, United States*

Received 15 May 2006; received in revised form 10 April 2007
Available online 3 July 2007

**Abstract**

A sharp interface technique is employed to study the interaction of a solid–liquid interface in a solidifying binary alloy with a ceramic particle in the melt. The application targeted is solidification of a metal–matrix composite. A level-set based sharp interface numerical method is used to study the directional solidification process in the presence of the particle. The transport of solute and heat are computed. The directional solidification calculations are first validated against stability theory. The Mullins–Sekerka stability spectrum is reproduced with good agreement with the theory. The interaction of the cellular interface with a ceramic particle in the melt is then computed. It is shown that, in contrast to the case of a pure material, the ratio of thermal conductivity of the particle to the melt plays no role in determining the front morphology and the result of the particle–front interaction. The diffusion of species controls the evolution of the phase front around the particle. The implications of the results for particle–front interactions in a binary alloy are discussed.


*Keywords:* Alloy solidification; Particle–front interactions

## 1. Introduction

Solidification front and particle interaction is very important to applications such as metal–matrix composites (MMCs) processing. Experiments show [1–3] that a particle that is approached by a (planar) solidification front can react in one of the following ways: (1) it may be pushed along with the moving front, (2) it may be engulfed in the front instantaneously, or (3) it may be pushed followed by engulfment. There are different theoretical models, mainly in pure melts, that purport to predict which one of the above three scenarios will occur. An overview of the experimental and theoretical work on front–particle interactions can be found in Asthana and Tewari [1] (see also [2,3]).

Most of the theoretical work on front–particle interaction has focused on the rather idealized, even contrived situation of the approach of a planar solidification front in a pure material towards a ceramic particle suspended in the melt. Furthermore, in these studies the front solidifies towards the particle at a controlled rate, by means of a directional solidification process. However, in actual casting processes of interest to MMC processing such idealized conditions are unlikely to be met. More realistic scenarios include solidification in the presence of pure undercooled melts or directionally solidified impure materials. In these situations, typically, the solidification front that approaches a particle assumes morphologies that are complex in shape, such as dendritic or cellular structures. Theoretical work on non-planar fronts interacting with particles has been lacking. Recently, Yang et al. [4] have computed the interaction of a non-planar solidification front with an embedded ceramic particle. They have shown that during dendrite–particle interactions, the particles will eventually be engulfed by the side branches, a mechanism that will lead to particles being segregated at grain boundaries in the final solid, rather than being located within the

* Corresponding author. Tel.: +1 319 384 0832; fax: +1 319 335 5669.
*E-mail address:* ush@icaen.uiowa.edu (H.S. Udaykumar).

0017-9310/$ - see front matter © 2007 Elsevier Ltd. All rights reserved.
doi:10.1016/j.ijheatmasstransfer.2007.04.037

grain. This form of particle inclusion in the solidified microstructure has been termed entrapment [5]. In a pure material, for both planar [6,7] and non-planar [4] morphologies, it has been shown that the particle-to-melt thermal conductivity ratio significantly influences the formation of the final shape of the dendrites and the composite microstructure. In this paper, we extend the study of Yang et al. [4] to examine the effect of solute transport during the solidification of a binary alloy on the interaction of a solid–liquid front with a ceramic particle placed ahead of it.

The basic ideas and quantitative details of the instability of solid–liquid interfaces, both for pure as well as alloy materials, are well established under well-defined growth conditions. In particular, the growth of crystals in undercooled pure melts and pattern selection during directional solidification of dilute binary alloys have been addressed in a quantitative way and are now part of classical pattern selection theory [8,9]. By performing linear stability analysis, Mullins and Sekerka [10] first proposed a stability criterion for a planar interface during directional solidification of a binary alloy. Following the Mullins–Sekerka analysis, several approaches have been employed to model and numerically simulate the directional solidification process in alloy melts [11–13]. Recently, Echebarria et al. [14], using a modified phase-field method with realistic parameters, showed that the Mullins–Sekerka stability spectrum can be captured successfully [14]. In order to achieve this result using the diffuse interface phase-field approach, Echebarria et al. [14] ensured that the phase-field model was cast in a form that balances the computational time and accuracy constraints. In the phase-field approach this is typically achieved by specifying the interface thickness parameter that produces the correct solutions in the sharp-interface limit while still maintaining reasonable computational times. An alternate way in which to compute the interfacial behavior in the directional solidification context is to use a sharp-interface representation. Some early work using boundary-fitted finite element methods was performed by Derby and Brown [15,16]. However, in recent years the phase-field model has been used more extensively than the sharp-interface approaches [17–20] to study alloy solidification at the micro-scale. Exceptions are the work by Udaykumar et al. [4,17,18] where a finite-difference fixed grid approach has been employed and that by Zhao et al. [19] who have used a finite element approach on fixed grids to compute the dendritic solidification phenomena. In this sharp-interface framework, no additional modeling aspects are involved beyond the conventional continuum transport equations and sharp interface jump and balance conditions. The current paper, as an extension of previous work [4,17] shows that by utilizing a level-set based sharp interface method, the Mullins–Sekerka stability spectrum during directional solidification can be reproduced accurately in a straightforward way. The method also enables simulation of the interactions of the cells grown from binary alloys under directional solidification settings with solid particles embedded in the melt. In this setting the temperature field has to be calculated (instead of supplied using the frozen temperature approximation) because the presence of the particle in front of the solidification interface distorts the thermal field around it. The methodology is outlined in Section 2, the numerical results are presented in Section 3 followed by a brief discussion in Section 4.

## 2. Formulation and computational approach

### 2.1. Governing equations

The computational setup adopted in the calculations is shown in Fig. 1. In order to save computational time, the domain is divided into two sub-domains: a fine mesh sub-domain OF and a stretched mesh sub-domain FL. In the fine mesh sub-domain, initially a solid seed crystal is placed at the left of the domain as illustrated in the figure. A small-amplitude sinusoidal perturbation of a specified wavelength is imposed at the center of the interface. To study front–particle interactions, a circular particle is embedded in the melt ahead of the front. The initial position of the solidification front is far enough away from the particle that the thermal and species fields are initially unhindered by the particle.

The thermal transport is solved using:

$$\frac{\partial T}{\partial t} = \alpha_{\mathrm{L/S/P}} \nabla^2 T \tag{1}$$

The $\alpha_{\mathrm{L/S/P}}$ are the thermal diffusion coefficients of the liquid (L), solid (S) and particle (P), respectively. $T$ denotes the temperature. For the present directional solidification process, the latent heat release at the solidification boundary is ignored in the calculations, i.e. it is assumed to diffuse much more rapidly than the rejected species and hence its transport is neglected as a significant effect. This affords the simplification that the heat flux balance condition applies at the solid–liquid interface is:

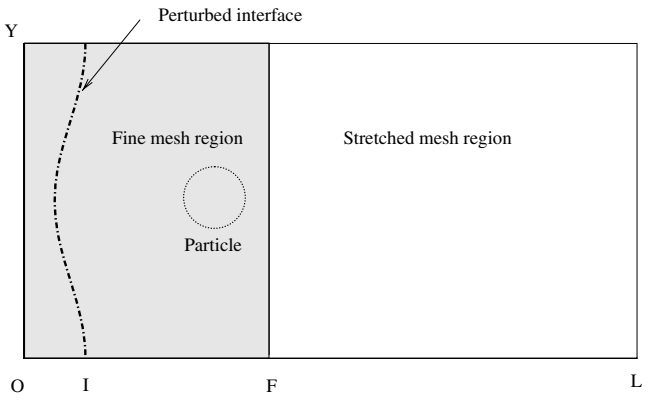


Fig. 1. Computational domain set up showing region of fine and coarse mesh, and initial front and particle positions. In simulations OY, OF and OL were varied depending on the perturbation wavelength chosen and the resolution provided by the mesh in each case.

$$K_S\left(\frac{\partial T}{\partial n}\right)_S = K_L\left(\frac{\partial T}{\partial n}\right)_L \tag{2}$$

where $K_{S/L}$ are the thermal conductivities of the solid and liquid, respectively. Note that if the condition in Eq. (2) is not assumed to apply, the Stefan condition must be satisfied at the interface in addition to Eq. (5). This renders the solution of the combined heat and solute transport equations rather stiff due to the disparate time scales of transport of latent heat and segregated species. In the current directional solidification setting, however, due to the large sensible heat transfer compared to the latent heat released at the interface, i.e. due to the typically large Stefan number, Eq. (2) is a reasonable assumption.

The heat flux balance condition at the particle–melt interface is:

$$K_L\left(\frac{\partial T}{\partial n}\right)_L = K_P\left(\frac{\partial T}{\partial n}\right)_P \tag{3}$$

where $K_P$ is the thermal conductivity of the particle.

The solute transport equation is solved in each phase:

$$\frac{\partial c}{\partial t} = D_{L/S/P}\nabla^2 c \tag{4}$$

The $D_{L/S/P}$ are the solutal diffusion coefficients inside the liquid, solid and the particle, respectively, and $c$ is the species concentration. The solute conservation equation at the solid–liquid interface is:

$$c_{L,int}(1-k)V_N = D_S\left(\frac{\partial c}{\partial n}\right)_S - D_L\left(\frac{\partial c}{\partial n}\right)_L \tag{5}$$

In the above, $c_{L,int}$ is the species concentration at the solid–liquid interface in the liquid, $V_N$ the interface velocity, and $k$ is partition coefficient so that:

$$c_{S,int} = kc_{L,int} \tag{6}$$

where $c_{S,int}$ is the species concentration at the solid–liquid interface in the solid. Since the species diffusion coefficient in the solid is usually orders of magnitude smaller than that in liquid and the first term of the right-hand side of Eq. (5) is typically small.

The interface temperature is related to the interface species concentration via the phase-diagram and is given by:

$$T_{int} = T_m - |m|c_{L,int} - \Gamma(1-15\varepsilon\cos(4\theta-\varphi))\kappa \tag{7}$$

where $T_{int}$ is the temperature at the interface, $T_m$ the melting temperature of the pure solvent, $m$ the liquidus slope, $\Gamma = \frac{\gamma T_m}{L}$ is the Gibbs–Thomson capillary coefficient, $\gamma$ is the surface tension, and $L$ is the latent heat of fusion per unit volume, $\kappa$ the interface curvature, $\varepsilon$ the anisotropy strength, $\theta$ the angle between the interface and the $x$-axis, $\phi$ the seed crystal orientation. The crystal is assumed to possess fourfold symmetry.

There is no species flux across the particle interface, i.e.:

$$\left(\frac{\partial c}{\partial n}\right)_P = 0 \tag{8}$$

The non-dimensional variables are defined as follows:

$$c^* = \frac{c - c_L^0}{c_L^0(1-k)}, \quad \Theta^* = \frac{T - T_m}{GD_L/V_p}, \quad x^* = \frac{x}{D_L/V_p},$$
$$t^* = \frac{t}{D_L/V_p^2}, \quad V_N^* = \frac{V_N}{V_p}, \quad \kappa^* = \frac{\kappa}{V_p/D_L} \tag{9}$$

In the above, the terms in the denominator are the scales of the respective quantities used to normalize the dimensional quantities. $G$ is the thermal gradient, $V_p$ the pulling velocity and the equilibrium concentration of the liquid at $T_0$ is:

$$c_L^0 = \frac{T_m - T_0}{|m|} \tag{10}$$

where $T_0$ is the interface temperature corresponding to the interface species concentration $c_\infty/k$, $c_\infty$ is the bulk concentration in the liquid and is also the steady state solid composition. The concentration in the solid phase at the interface is obtained from Eq. (6).

The non-dimensional equations then are:

$$\frac{\partial \Theta^*}{\partial t^*} = \frac{\alpha_{S/L/P}}{D_L}\nabla^2\Theta^* \tag{11}$$
$$\frac{\partial c^*}{\partial t^*} = \frac{D_{L/S/P}}{D_L}\nabla^2 c^* \tag{12}$$
$$\left[1+(1-k)c_L^*\right]V_N^* = \frac{D_S}{D_L}\left(\frac{\partial c^*}{\partial n^*}\right)_S - \left(\frac{\partial c^*}{\partial n^*}\right)_L \tag{13}$$
$$\frac{K_S}{K_L}\left(\frac{\partial \Theta^*}{\partial n^*}\right)_S = \left(\frac{\partial \Theta^*}{\partial n^*}\right)_L \tag{14}$$
$$\frac{K_L}{K_P}\left(\frac{\partial \Theta^*}{\partial n^*}\right)_L = \left(\frac{\partial \Theta^*}{\partial n^*}\right)_P \tag{15}$$
$$\left(\frac{\partial c^*}{\partial n^*}\right)_P = 0 \tag{16}$$
$$c_{L,int}^* = \Xi - \Phi\Omega - \Psi\kappa^* \tag{17}$$

where

$$\Xi = -\frac{1}{1-k}, \quad \Phi = \frac{GD_L}{|m|c_L^0 V_p(1-k)},$$
$$\Omega = \Theta_{int}^*, \quad \text{and} \quad \Psi = \frac{\Gamma(1-15\varepsilon\cos(4\theta-\varphi))V_p}{|m|c_L^0 D_L(1-k)} \tag{18}$$

The above symbols represent, respectively, dimensionless bulk concentration, temperature gradient, interface temperature and capillary supercooling. The steady state species concentration field is used as the initial condition, so that in the solid:

$$c = c_L^0 k \quad \text{or} \quad c^* = -1 \tag{19}$$

While in the liquid, the initial condition is:

$$c = c_L^0 k + (c_L^0 - c_L^0 k)\exp\left(-\frac{V_p x}{D_L}\right) \quad \text{or}$$
$$c^* = -1 + \exp(-V_p^*(x^* - R^*)) \tag{20}$$

where $R^*$ is the initial solidification interface location.

*The frozen temperature approximation*: To validate the current method, the computed results are first compared

against the Mullins–Sekerka instability theory. To perform such an analysis, instead of using a heat conduction equation to calculate the temperature field, the frozen temperature approximation is adopted, as is done by Echebarria et al. [14]. This assumption is typically applied in directional solidification experiments due to the high Lewis number ($Le = \alpha/D$) and the small sample thicknesses relative to sample length. For a solidification front advancing along the $x$-direction (see Fig. 1), the temperature anywhere in the field can then be calculated using the frozen temperature approximation as:

$$T = T_0 + G(x - V_p t) \tag{21}$$

Eq. (7) then becomes:

$$c_{L,int}/c_L^0 = 1 - (1-k)d_0\kappa - (1-k)(x - V_p t)/l_T \tag{22}$$

where

$$d_0 = \frac{\Gamma}{\Delta T_0} \tag{23}$$

is a capillary length, $\Delta T_0 = |m|(1-k)c_L^0$ the freezing range, and

$$l_T = \frac{|m|(1-k)c_L^0}{G} \tag{24}$$

the thermal length scale.

Now Eq. (22) can be employed to compute the interface species composition. The interface velocity can then be obtained using Eq. (13).

Using the same non-dimensional variables defined in Eq. (9), the non-dimensional equation set in the case of the frozen temperature approximation stays the same except that the parameters in Eq. (17) become:

$$\Xi = 0, \Omega = x^* - V_N^* t^* \tag{25}$$

The other two parameters $\Phi$ and $\Psi$ in Eq. (17) are the same as defined in Eq. (18).

*Mullins–Sekerka instability growth rate*: To compute the response of the interface to disturbances, a perturbation is applied to the interface in the form $\delta\sin(\omega y - \pi/2)$ where $\delta$ is the amplitude of the perturbation and $\omega$ is the wavenumber. Mullins–Sekerka instability theory [10] predicts that the growth rate of the perturbation will be:

$$\chi = \frac{\dot{\delta}}{\delta} = \frac{V\omega\{-2T_M\Gamma\omega^2[\omega^* - (V/D)p] - (\varsigma' + \varsigma)[\omega^* - (V/D)p] + 2mG_c[\omega^* - (V/D)]\}}{(\varsigma' - \varsigma)[\omega^* - (V/D)p] + 2\omega mG_c} \tag{26}$$

In the above, in the interest of brevity the symbols $\varsigma = [2K_L/(K_S + K_L)]G$ and $\varsigma' = [2K_S/(K_S + K_L)]$ have been employed, $K_S$, $K_L$ are the thermal conductivity of the solid and liquid, respectively, $p = 1 - k$, $\omega^* = (V/2D) + [(V/2D)^2 + \omega^2]^{1/2}$ and $mG_c = -(V/D)mc_\infty \times [(1-k)/k]$. In the present case of frozen temperature approximation, the temperature gradients in the liquid and the solid are the same, so that $\varsigma' = \varsigma = G$. The simplified equation then reads:

$$\chi = \frac{\dot{\delta}}{\delta} = \frac{V\{-T_M\Gamma\omega^2[\omega^* - (V/D)p] - G[\omega^* - (V/D)p] + mG_c[\omega^* - (V/D)]\}}{mG_c} \tag{27}$$

This equation is used to predict the perturbation growth rate for directional solidification without anisotropy at the interface. With anisotropy, the Gibbs–Thomson coefficient becomes $\Gamma(1 - 15\varepsilon\cos(4\theta - \varphi))$ in the cases studied, where $\varepsilon$ is the anisotropy strength.

### 2.2. Computational technique

The computational approach is described in detail in [17]. A narrow-band level-set [21] is used to represent the embedded interface, i.e. the solidification front. The governing equations are discretized using the techniques described in [17]. Briefly, a second-order accurate finite-difference scheme is employed to discretize the governing equations. The equations are solved on a fixed Cartesian grid and the embedded interfaces (the solid–liquid interface and the particle-liquid interface) are treated as sharp entities that move through the fixed mesh. The presence of the interface is accounted for by using the level-set field to redefine the discretization stencil at computational points that straddle the interface. This simplifies immensely the task of developing a sharp-interface methodology for complex interfaces. The methodology has been carefully benchmarked [17] and the dendrites computed have been shown to match very well with theoretical predictions of tip characteristics from solvability theory.

### 2.3. Interfacial conditions

There are two interfaces, i.e. the solidification front and the particle–melt interface, where balance conditions must be applied. The heat flux balance condition, Eq. (15), is used to calculate the particle interfacial temperature. The gradients in Eq. (15) are expressed in discrete form using the normal probe technique [4], and the gradient on the liquid side can be written as:

$$\left(\frac{\partial\Theta^*}{\partial n^*}\right)_L = 2\Theta_{L1}^* - \frac{1}{2}\Theta_{L2}^* - \frac{3}{2}\Theta_{int}^* \tag{28}$$

where $\Theta_{L1}^*$ and $\Theta_{L2}^*$ are the temperature values at the first and second probe point in liquid, respectively. These probe

points are obtained in the direction normal to the interface and placed at distances of $\Delta x$ from the interface, as illustrated in Fig. 2. The point at the interface is denoted by N in Fig. 2. Using the level-set field information its location is given by:

$$\vec{x}_{\mathrm{N}} = \vec{x}_{i,j} - \vec{n}_{i,j}(\phi_l)_{i,j} \tag{29}$$

where $\vec{n}_{i,j}$ is the unit normal from the point $(i,j)$ to the interface, and $(\phi_l)_{i,j}$ is the level-set value at the point $(i,j)$. The locations of the probe points in liquid and particle phases can be calculated using the following:

$$\vec{x}_{\mathrm{L1}} = \vec{x}_{\mathrm{N}} + \vec{n}_{\mathrm{N}}\,\mathrm{d}x_{\mathrm{L1}} \tag{30a}$$

$$\vec{x}_{\mathrm{L2}} = \vec{x}_{\mathrm{N}} + \vec{n}_{\mathrm{N}}\,\mathrm{d}x_{\mathrm{L2}} \tag{30b}$$

$$\vec{x}_{\mathrm{P1}} = \vec{x}_{\mathrm{N}} - \vec{n}_{\mathrm{N}}\,\mathrm{d}x_{\mathrm{P1}} \tag{30c}$$

$$\vec{x}_{\mathrm{P2}} = \vec{x}_{\mathrm{N}} - \vec{n}_{\mathrm{N}}\,\mathrm{d}x_{\mathrm{P2}} \tag{30d}$$

Bilinear interpolation is performed from the surrounding mesh points to obtain the value of the variable $\Theta$ at points $\vec{x}_{\mathrm{L1}}, \vec{x}_{\mathrm{L2}}, \vec{x}_{\mathrm{P1}}, \vec{x}_{\mathrm{P2}}$. The unit normal vector at $N$, $\vec{n}_{\mathrm{N}}$ is also obtained by bilinear interpolation from the surrounding mesh points [4]. The distance from probe points to interface is: $\mathrm{d}x_{\mathrm{L1}} = \mathrm{d}x_{\mathrm{P1}} = \Delta x$ and $\mathrm{d}x_{\mathrm{L2}} = \mathrm{d}x_{\mathrm{P2}} = 2\Delta x$. (The temperature gradient at the solid–liquid interface $\left(\frac{\partial \Theta}{\partial n}\right)_{\mathrm{S/L}}$ in Eq. (14) can be obtained in a similar way.) Thus, the resulting interfacial temperature is then computed from:

$$\Theta^*_{\mathrm{int}} = \frac{4(K_{\mathrm{L}}\Theta^*_{\mathrm{L1}} - K_{\mathrm{P}}\Theta^*_{\mathrm{P1}}) - (K_{\mathrm{L}}\Theta^*_{\mathrm{L2}} - K_{\mathrm{P}}\Theta^*_{\mathrm{P2}})}{3(K_{\mathrm{L}} - K_{\mathrm{P}})} \tag{31}$$

where $\Theta^*_{\mathrm{P1}}$ and $\Theta^*_{\mathrm{P2}}$ are the temperature values at the first and second probe point in the particle, respectively.

When the solidification front approaches close to the solid particle the two normal probe points required to extract gradient information in Eq. (28) may no longer lie in the liquid phase. Therefore, when contact between the solidification front and the particle is imminent special treatment is needed to update the motion of the solidification front. In the current framework, using the level-set information, it is a simple matter to detect when this type of situation arises. For example, once the probe point locations are determined (Eqs. (30a) and (30b)) for the solidification front on the liquid side, the value of the level-set defining the particle is computed at that point (using a bilinear interpolation) from the surrounding grid points. If the level-set value (for the particle) at that point happens to be negative then that probe point lies inside the particle and therefore is not available for computation of the gradient in Eq. (28). When only the second probe point P2 lies inside the particle but P1 lies in the liquid, then as demonstrated in Fig. 3a, the gradient is obtained using only one probe point in the liquid phase. This leads to a 1st order estimate for the gradient. In this case, only two points, i.e. the first probe P1 and interface point N are available for calculation of the temperature gradient. As the gap between the dendrite and the particle narrows and the first probe point P1 is also inside the particle, then contact is considered to have occurred, i.e. the gap between the front and particle is less than one grid spacing. Thus, the first probe point is now placed on the point M2 (Fig. 3b) which lies on the particle surface and the two interface points N and M2 are used to obtain the normal gradient of the temperature. The particle interface point M2 is located at:

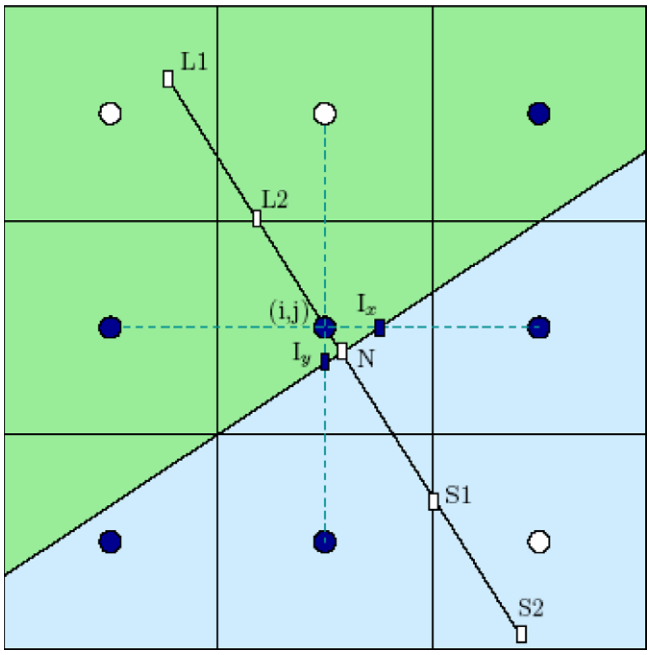


Fig. 2. Method for evaluating the normal gradients at the interface. The point on the interface is designated N and the probe points are shown in the liquid (L1 and L2) and solid phases (S1 and S2).

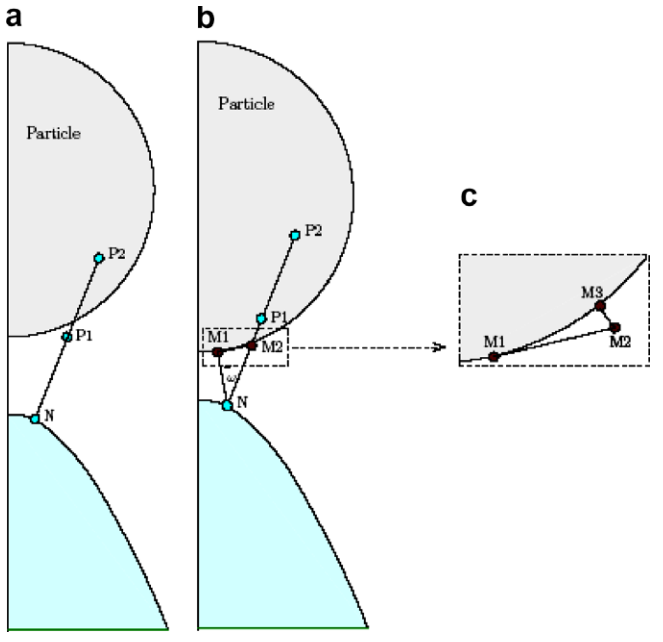


Fig. 3. The case of approach of a solidification front towards a particle. Determination of gradients of temperature/species when: (a) the second probe point is in a different phase, (b) the first probe point is in a different phase, and (c) amplified view of the box from (b).

$$\vec{x}_{M2} = \vec{x}_N + \vec{n}_N \, dx_{NM2} \tag{32}$$

where the distance $dx_{NM2}$ is given by:

$$dx_{NM2} = \frac{(\phi_P)_N}{\cos\bar{\omega}} \tag{33}$$

where $(\phi_P)_N$ is the value of the distance function corresponding to the particle surface computed at the point N, i.e. the distance |M1N| as illustrated in Fig. 3b, and $\bar{\omega}$, the angle ∠M1NM2 as illustrated in Fig. 3b, is given by:

$$\bar{\omega} = \mathrm{ATAN}\left\{\mathrm{ABS}\left[\frac{(n_y)_P}{(n_x)_P} - \frac{(n_y)_F}{(n_x)_F}\right]\right\} \tag{34}$$

In Eq. (34) $(n_{y/x})_P$ is the $y/x$ component of the normal to the particle surface (i.e. computed from the level-set field defining the particle surface) computed at the solid–liquid interface point N. Similarly $(n_{y/x})_F$ is the $y/x$ component of the normal to the solidification front computed at point N. In general, due to the curvature of the particle surface the point M2 will not lie exactly on the particle surface. Therefore the closest point on the particle surface, denoted M3 in Fig. 3c is identified and the temperature at that point is chosen as the particle surface temperature. This point M3 can be easily located (see illustration in Fig. 3c) using the following equation:

$$\vec{x}_{M3} = \vec{x}_{M2} + \vec{n}_{M2}(\phi_P)_{M2} \tag{35}$$

where $\vec{n}_{M2}$ is the normal at point M2 with respect to the particle interface.

The value of the temperature at the point M3 is obtained from the heat flux balance at the particle surface. This is described below.

The solid–liquid interface is taken to be in perfect thermal contact in the situation illustrated in Fig. 3b. Therefore, when the gap between the phase boundary and the particle is less than a grid spacing the temperature at point N is taken to be equal to that at the point M3. Then, the following conditions are satisfied:

$$\Theta_N = \Theta_{M3} \tag{36}$$

and heat flux balance:

$$k_P\left(\frac{\partial\Theta}{\partial n}\right)_P = k_S\left(\frac{\partial\Theta}{\partial n}\right)_S \tag{37}$$

In discrete form the above equation is:

$$k_P\left(2\Theta_{P1} - \frac{1}{2}\Theta_{P2} - \frac{3}{2}\Theta_{M3}\right) = k_S\left(2\Theta_{S1} - \frac{1}{2}\Theta_{S2} - \frac{3}{2}\Theta_N\right) \tag{38}$$

Using Eqs. (36) and (38):

$$\Theta_N = \Theta_{M3} = \frac{4(k_S\Theta_{S1} - k_P\Theta_{P1}) - (k_S\Theta_{S2} - k_P\Theta_{P2})}{3(k_S - k_P)} \tag{39}$$

Here the values of temperature in the particle and solid, i.e. $\Theta_{P1}$, $\Theta_{P2}$ and $\Theta_{S1}$, $\Theta_{S2}$, respectively, are again computed using bilinear interpolation from the surrounding grid points.

The zero-flux condition, i.e. Eq. (16) is applied on the species concentration in the melt at the particle surface. The discretization of the species balance condition follows essentially along the lines of the temperature gradient calculations described above.

At the solid–liquid interface, the interface temperature is obtained based on the assumption that latent heat release can be neglected. This implies that Eq. (14) applies for the interface temperature, which can be treated in a manner similar to that for Eq. (15), which is described above. Eq. (13) is used to calculate the species composition in the liquid phase and the solid phase species composition is computed using Eq. (6).

## 3. Results

### 3.1. Material 1: succonitrile–acetone

In the first set of cases, the commonly employed model material, succinonitrile (SCN)–acetone binary alloy, was used as the material to be solidified. Computations of the solidification process were carried out with imposed small perturbations on the interface to generate the Mullins–Sekerka stability spectrum. The values of pulling speed, imposed temperature gradient and other parameters are given in Table 1. The computational domain is shown in Fig. 1 (there is no particle in the present case). A fine mesh was adopted in the shaded region $O < x < F$ in Fig. 1, and a stretched mesh was used in region $F < x < L$. The mesh spacing in the fine mesh region was determined by performing a mesh refinement study and based on previous analyses [17] of mesh density requirements to achieve grid independence. I is the solidification front location. A perturbation was imposed onto the solid–liquid interface at the beginning as illustrated in Fig. 1. In the simulations, the perturbation amplitude was such that it lay within a mesh cell. The subsequent growth of this perturbation was followed to determine the growth rate. Seven different wavenumbers were used to reproduce the Mullins–Sekerka

Table 1
Parameters for the binary succinonitrile (SCN)–acetone alloy system of Ref. [22] and Al–Cu alloy system from Ref. [21] used in the directional solidification simulations

| Material properties | SCN–acetone | Al–Cu |
|---|---|---|
| $\lvert m\rvert c_\infty$ (shift in melting temperature) | 2 K | 7.8 K |
| $D_L$ (species diffusion coefficient) | 1000 μm²/s | 3000 μm²/s |
| $\Gamma$ (Gibbs–Thomson coefficient) | $6.48 \times 10^{-2}$ K μm | $2.4 \times 10^{-1}$ K μm |
| $V_p$ (pulling speed) | 32 μm/s | 3000 μm/s |
| G (thermal gradient) | $1.4 \times 10^{-2}$ K/μm | 0.56 K/μm |
| $d_0$ (capillary length) | $1.3 \times 10^{-2}$ μm | $5 \times 10^{-3}$ μm |
| $l_T$ (thermal length) | $3.33 \times 10^{2}$ μm | $3.42 \times 10^{4}$ μm |
| $l_D$ (species diffusion length) | 60 μm | 60 μm |
| $k$ (partition coefficient) | 0.3 | 0.14 |

Table 2
Computed results for the Mullins–Sekerka stability spectrum where $d_0 = 1.3 \times 10^{-2}$ μm, $l = 2D/V_p$, $\eta$ the wave number, $\eta l$ the dimensionless wave number, and $\chi$ the growth rate

| | | | | | | | |
|---|---|---|---|---|---|---|---|
| $\eta$ ($10^{-3} d_0$) | 2.513 | 5.027 | 7.854 | 10.47 | 12.57 | 15.71 | 17.95 |
| $\eta l$ | 12.083 | 24.166 | 37.760 | 50.346 | 60.415 | 75.517 | 86.307 |
| $\chi l^2/2D$ ($\varepsilon = 0$) | 10.935 | 20.025 | 27.68 | 31.004 | 29.576 | 20.683 | 4.703 |
| $\chi l^2/2D$ ($\varepsilon = 0.007$) | 10.935 | 20.295 | 28.365 | 32.680 | 32.190 | 25.495 | 12.563 |

stability spectrum. The wavenumbers chosen are given in Table 2.

Before the Mullins–Sekerka stability spectrum was reproduced a mesh independence study was carried out. The highest wave number among the seven wave numbers was chosen for the convergence study, since it is the most unstable situation that is encountered in the simulations. If a mesh is fine enough to adequately resolve the highest wave number case, it may be expected to be fine enough for the other cases as well. In this case the wave number $\eta = 1.795 \times 10^{-2} d_0$ and the non-dimensional wave number $\eta l = 86.307$; the perturbation amplitude $\delta = 0.0039$ μm, which in non-dimensional terms is $\delta^* = 0.0003$. The (non-dimensional) mesh sizes chosen were $\Delta x = 0.002$, 0.003, 0.005, 0.01. The imposed initial perturbation is only a small fraction of a mesh spacing in amplitude. As described in previous work [4] the time step sizes are chosen to correspond to a CFL-type criterion based on the maximum interface velocity and therefore the computational times vary depending on the problem. In each case, the typical computational times for the development of the full instabilities, i.e. into the deeply nonlinear regime, required computational (CPU) times of the order of a few hours. The $y$-direction domain length is OY = 18, which corresponds to half of a wave length. The results for the convergence study are presented in Fig. 4. The mesh size convergence study above shows that for a mesh size $\Delta x = 0.005$, the result is already very close to the $\Delta x = 0.002$ result. The fact that the results from mesh sizes $\Delta x = 0.002$, and 0.003 are almost identical implies that convergence with grid refinement was achieved for these mesh spacings.

The Mullins–Sekerka linear stability analysis leads to the expression for growth rate for small perturbations as a function of the disturbance wavelength as given in Eq. (27). The function is plotted in Fig. 5 for the case of isotropic surface tension as well as for anisotropic surface tension with anisotropy strength $\varepsilon = 0.007$. The numerical results are presented in Table 2 for use as benchmarks. The growth rate values were determined by recording the amplitude of the perturbation with time and fitting an exponential curve to determine the growth rate, i.e. by expressing $\delta = A \cdot \exp(B + C)$, where $A$, $B$ and $C$ are parameters to be determined. The amplitude growth rate $\chi = \dot{\delta}/\delta$ then obtained from the parameter $B$.

The results for the stability spectrum for the isotropic as well as anisotropic cases are shown in Fig. 5 where the lines correspond to the amplification rate given by theory and the symbols are the computed results. The computed amplification rates are in excellent agreement with theory over the entire range of wavenumbers studied.

Calculations of the interfacial instability were then carried into the nonlinear regime. For the conditions of the study, the planar interface is expected to transition to a cellular morphology as the instability of the solidification front continues to develop. In order to observe this transition, case 1 of Table 2 is run for long times keeping all other parameters unchanged. The small perturbation then grows into the cellular shape shown in Fig. 6a. Fig. 6b shows the concentration field around the cell, and Fig. 6c

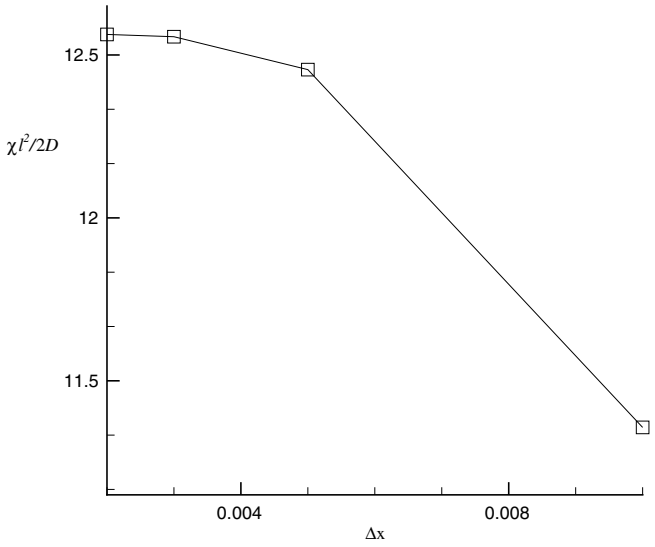


Fig. 4. Computed results for the non-dimensional perturbation growth rate against mesh size. Convergence with grid refinement is observed as the mesh size decreases.

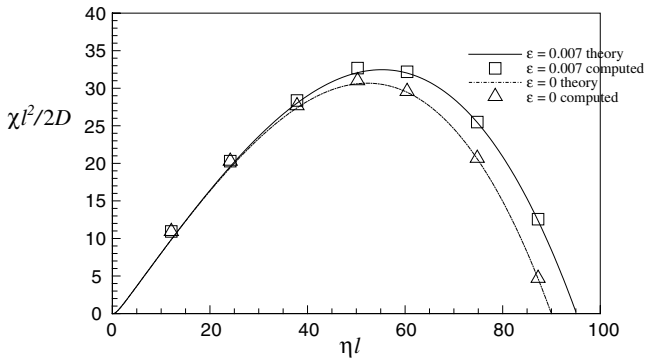


Fig. 5. The nondimensional growth rate plotted against the dimensionless wave numbers, for cases with and without anisotropy ($\varepsilon$) of interfacial tension.

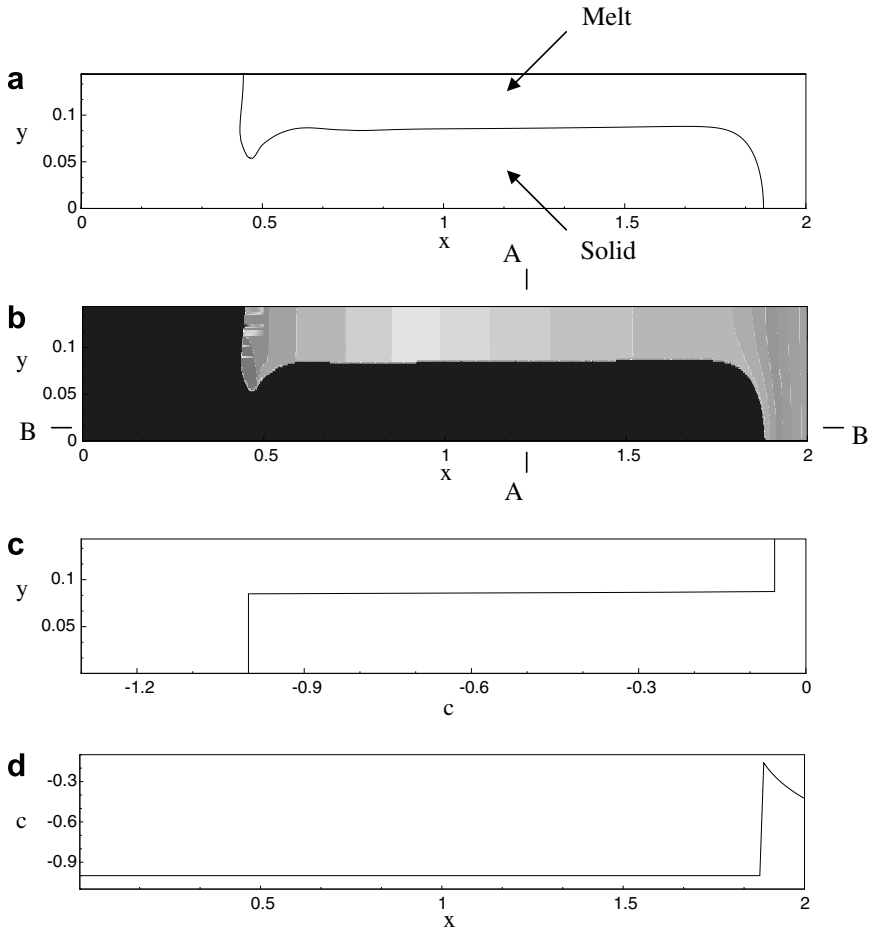


Fig. 6. The cellular growth of solidification front during directional solidification, SCN–acetone with anisotropy $\varepsilon = 0.007$. (a) Cell profile; (b) species concentration contours; (c) species concentration profile extracted across section A–A; (d) species concentration profile extracted across section B–B.

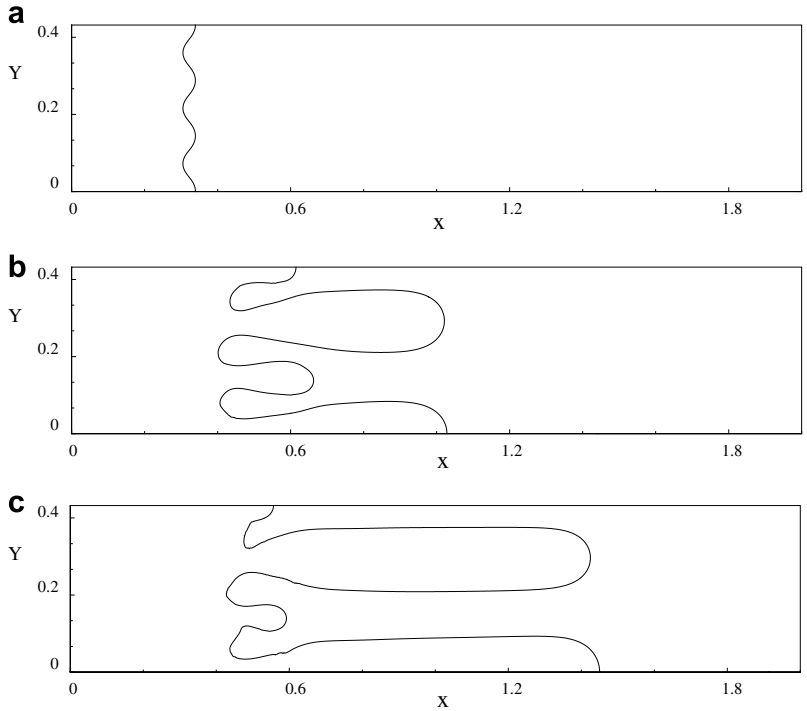


Fig. 7. The cellular growth during directional solidification of SCN–acetone, with a initial perturbation of three full wavelengths, with anisotropy $\varepsilon = 0.007$ (a) initial time (early growth phase of the perturbations), (b) intermediate time, and (c) later time showing mature cells and wavelength selection.

shows the concentration profile along the section A–A illustrated in Fig. 6b. Fig. 6d shows the concentration profile along the section B–B illustrated in Fig. 6b. As illustrated by Fig. 6, in the present sharp interface technique, the species composition changes abruptly across the interface, and the microsegregation of solute into the liquid phase is captured without any smearing at the solid–liquid interface. Furthermore, consistent with theory [22,23], the cellular shape selected in the present case achieves a final quasi-steady shape that occupies roughly half the lateral extent of the domain of growth. The cell spacing in this case is constrained by the boundary conditions applied on the sides of the domain (i.e. at $y = 0$ and $y = Y$, both of which are symmetry boundaries). To determine whether the final cell width is robust or whether it is dictated by the lateral extent and boundary conditions of the computational domain a further investigation was carried out by keeping all the parameters used in Fig. 6 the same, except that the lateral extent of the domain was increased. The height OY of the computational domain in this case is such that three wavelengths of the perturbation are accommodated. The results (Fig. 7a) show that the perturbation initially grows such that the four tips amplify at the same rate, while later in the evolution numerical noise leads to the selection of two of the tips into full-grown cells while the other tips atrophy. The width of the final cells observed match that of the cell shown in Fig. 6 indicating that the selected spacing is robust for the imposed growth conditions and material parameters.

### 3.2. Material 2: Al–Cu alloy

As a second material, an Al–Cu alloy was used to investigate the cellular growth in directional solidification. The system of equations solved is the same as for the SCN–acetone material above. The difference between the two systems lies in the non-dimensional parameters $\Phi$ and $\Psi$. For the Al–Cu parameters listed in Table 1 [24] yields $\Phi = 4.2576 \times 10^{-3}$ and $\Psi = 1.16875 \times 10^{-3}$. The previously computed SCN–acetone cases, however, used values of $\Phi = 3.9769 \times 10^{-4}$ and $\Psi = 9.375 \times 10^{-2}$. Thus, in the present case the values of the non-dimensional parameters $\Phi$ and $\Psi$ are, respectively, higher and lower than that of the SCN–acetone system. This implies that the driving force for the instability is higher and the surface tension is lower in the present case when compared to the previous one. It is expected that the observed features of the instability will be finer in the present case.

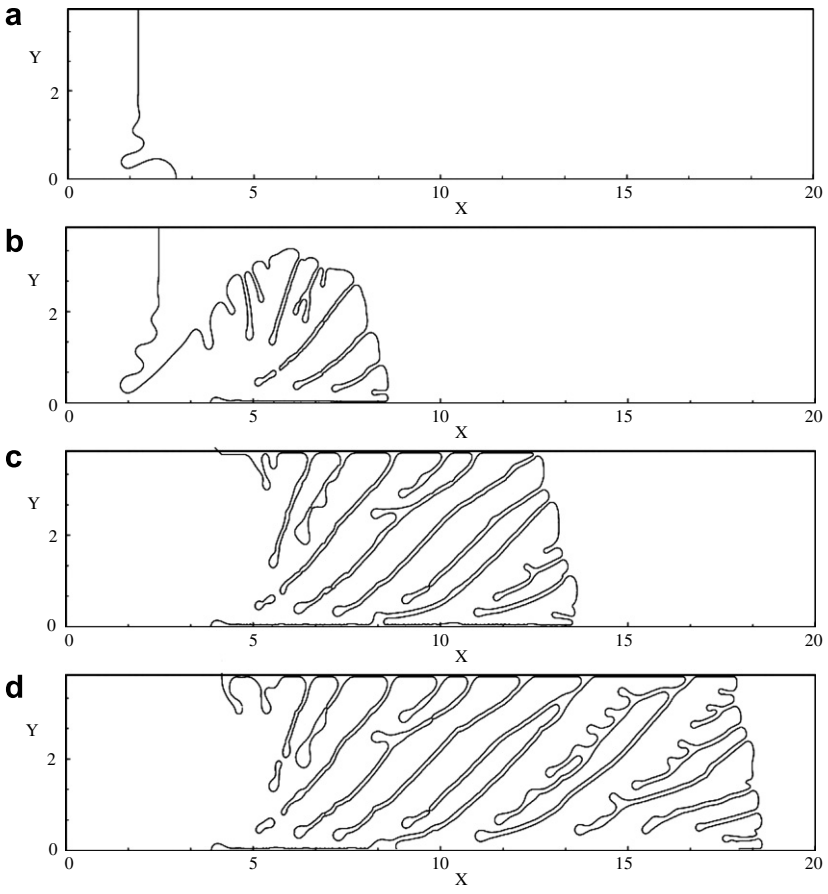


Fig. 8. Cellular growth of the Al–Cu alloy. Cell growth begins from bottom left of the domain and the cells grow to occupy the whole domain (a) beginning stages; (b) intermediates stage showing spread of the cellular structure to occupy space; (c) intermediate stage showing growth of the cellular structures to the right; and (d) later stage showing wavelength readjustment by instabilities of the original cell, cell–cell competition and tip-splitting. The overall interface now is nearly planar.

The computational domain adopted is as illustrated in Fig. 1. The cases in this section do not include a particle in the melt ahead of the front. The domain sizes are specified as the following: OY = 4, OL = 40 with the fine mesh region OF = 20. The mesh size is $\Delta x = 0.005$ and is selected based on the grid refinement studies presented earlier. The parameters used for the Al–Cu alloy directional solidification are given in Table 1. The initial half wavelength of a sinusoidal perturbation is given at the bottom left corner. The results are presented in Fig. 8 (notice that only results of fine mesh domain is shown in this plot). The perturbation develops at the bottom left into a cellular protuberance. The cell then keeps splitting to form new cells to occupy space when it grows toward the right. After the cells reach the upper wall, all the cells grow to the right, and in the end, the overall interface tends to become flat again. Thus, as expected, the present case is much more unstable than the previous case using the SCN–acetone alloy. The mechanisms for wavelength adjustment, namely tip-splitting of cells, interfacial instability of the sides of cells to generate sidearms [25] that mature into full cells as they grow and the competition between cells, are all observed in Fig. 8.

### 3.3. Effect of a ceramic particle on front propagation

The Al–Cu alloy is used to study the interaction of a directionally solidifying front with an embedded ceramic particle. The material properties and parameters, such as the directional solidification (pull) velocity and temperature gradient employed in the simulations are given in Table 1. The computational domain is as shown in Fig. 1. A fine mesh is adopted in region OF and the mesh is linearly stretched in region FL. Figs. 9–13 show the simulation results of the interactions of particles with develop-

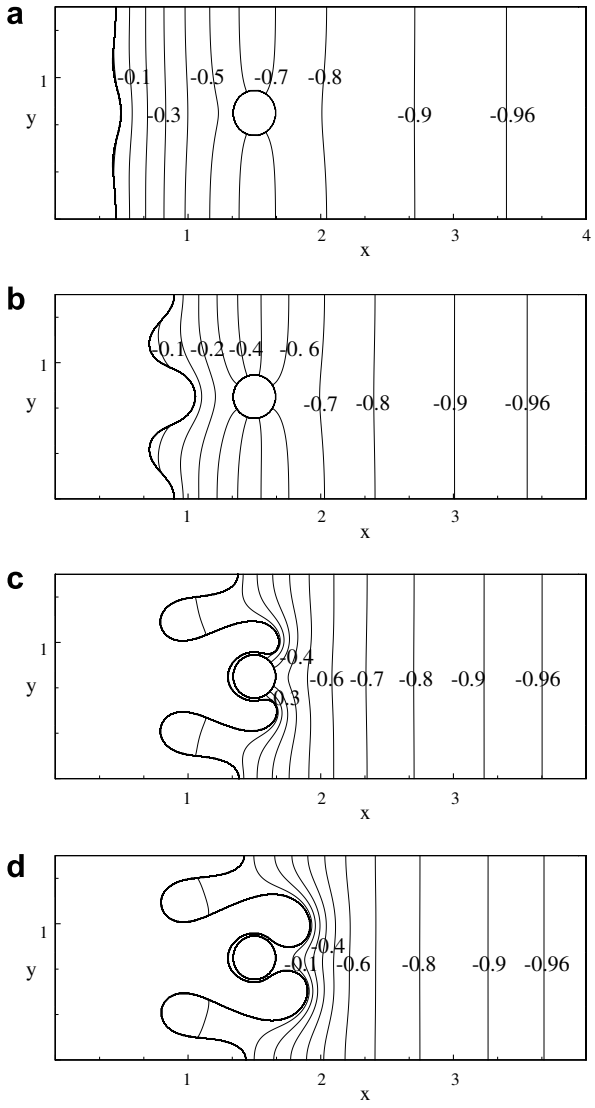


Fig. 9. The species concentration contours shown at different times for the directional solidification process in the presence of a ceramic particle ($k_P/k_L = 0.01$). The interface shape and non-dimensional species concentration are shown at four different instants during the development of the instability.

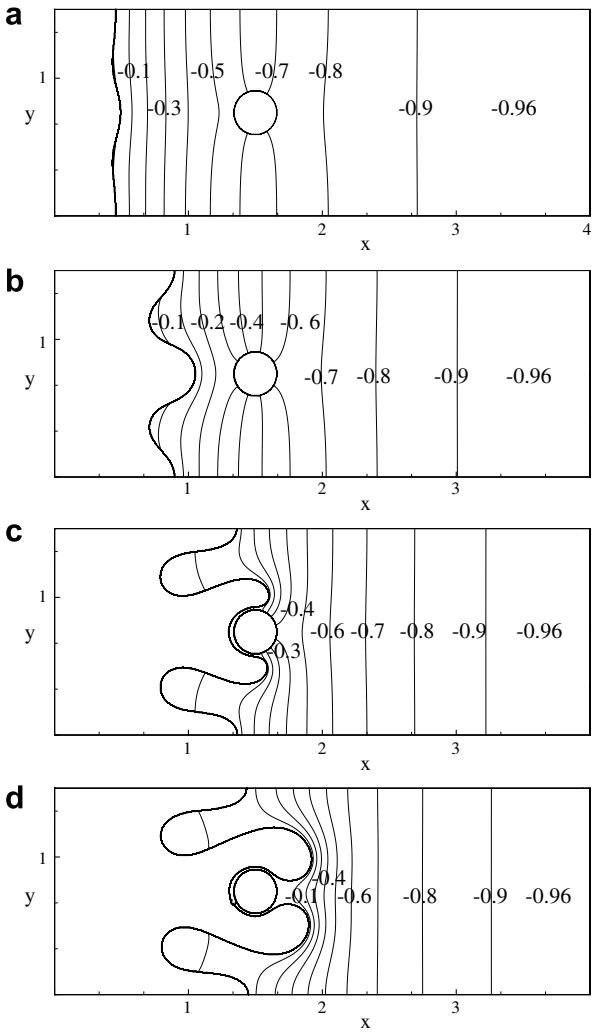


Fig. 10. The species concentration contours shown at different times for the directional solidification process in the presence of a ceramic particle ($k_P/k_L = 1.0$). The interface shape and non-dimensional species concentration are shown at four different instants during the development of the instability.

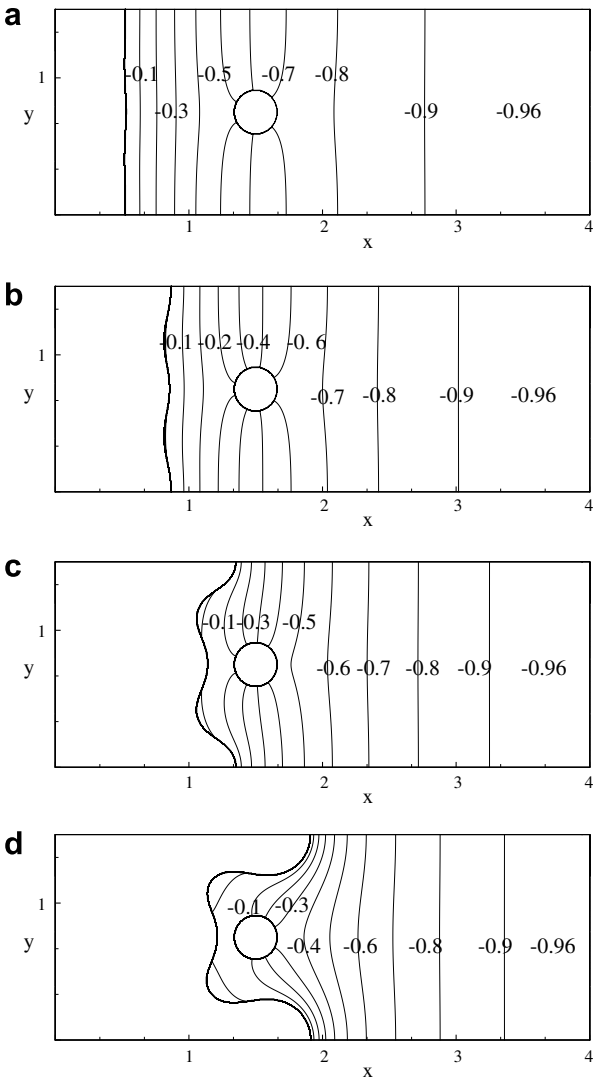


Fig. 11. The species concentration contours (for a low growth rate wavenumber for the initial perturbation) shown at different times for the directional solidification process in the presence of a ceramic particle ($k_P/k_L = 0.01$). The interface shape and non-dimensional species concentration are shown at four different instants during the development of the instability.

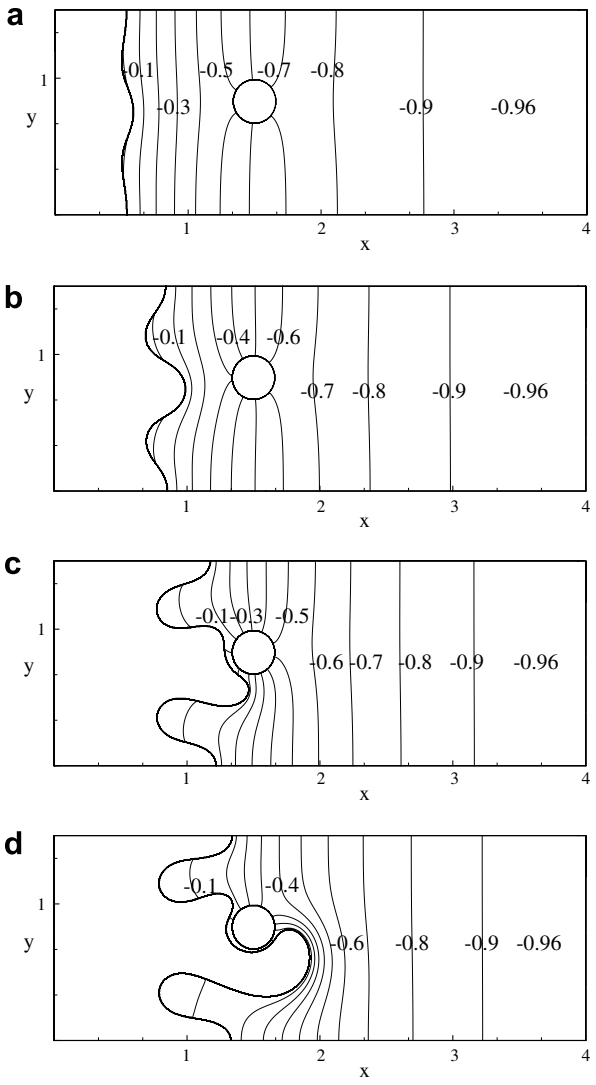


Fig. 12. The species concentration contours (for a front approaching a particle asymmetrically) shown at different times for the directional solidification process in the presence of a ceramic particle ($k_P/k_L = 0.01$). The interface shape and non-dimensional species concentration are shown at four different instants during the development of the instability.

ing cells. In these simulations the fine mesh sub-domain is $2 \times 1.5$ units and a $500 \times 375$ uniform mesh ($\Delta x = \Delta y = 0.004$) is employed; the overall domain is $4 \times 1.5$ units using a ($560 \times 375$) mesh. Fig. 9 shows the evolution of the solidification front to form a steadily growing cell when interacting with a particle placed ahead of it. The particle diameter is 0.25 dimensionless units, so that 50 mesh points lie within the particle. The particle is therefore well resolved by the mesh. Because of the initial perturbation, Fig. 9a shows that the interface becomes unstable, a cell starts to grow out of the perturbed area; Fig. 9b shows that the cell continues to grow until it reaches the particle. Fig. 9c shows the particle obstructs the solutal diffusion in front of the cell. This leads to accumulation of the solute between the particle and the growing cell, resulting in a high species concentration in the gap. The driving force for solidification which is the species concentration gradient progressively decreases beneath the particle. The cell starts to grow around the particle following the direction of the highest solutal gradients, i.e. the imposed thermal gradient is overridden. Finally, Fig. 9d shows the cell grows completely around the particle and a particle engulfment results.

Yang et al. [4] showed that for pure material, when a growing dendrite interacts with solid particles, the particle melt thermal conductivity ratio $k_P/k_L$ is crucial in determining the behavior of the dendrite. When $k_P/k_L < 1$, as the growing dendrite grows towards the particle, there is a layer of warm liquid that forms between the particle and the dendrite. Therefore the dendrite tip is slowed down and the dendrite tip radius is enlarged as the particle is approached. In the impure material case, since the interface velocity is determined mainly by the species concentration

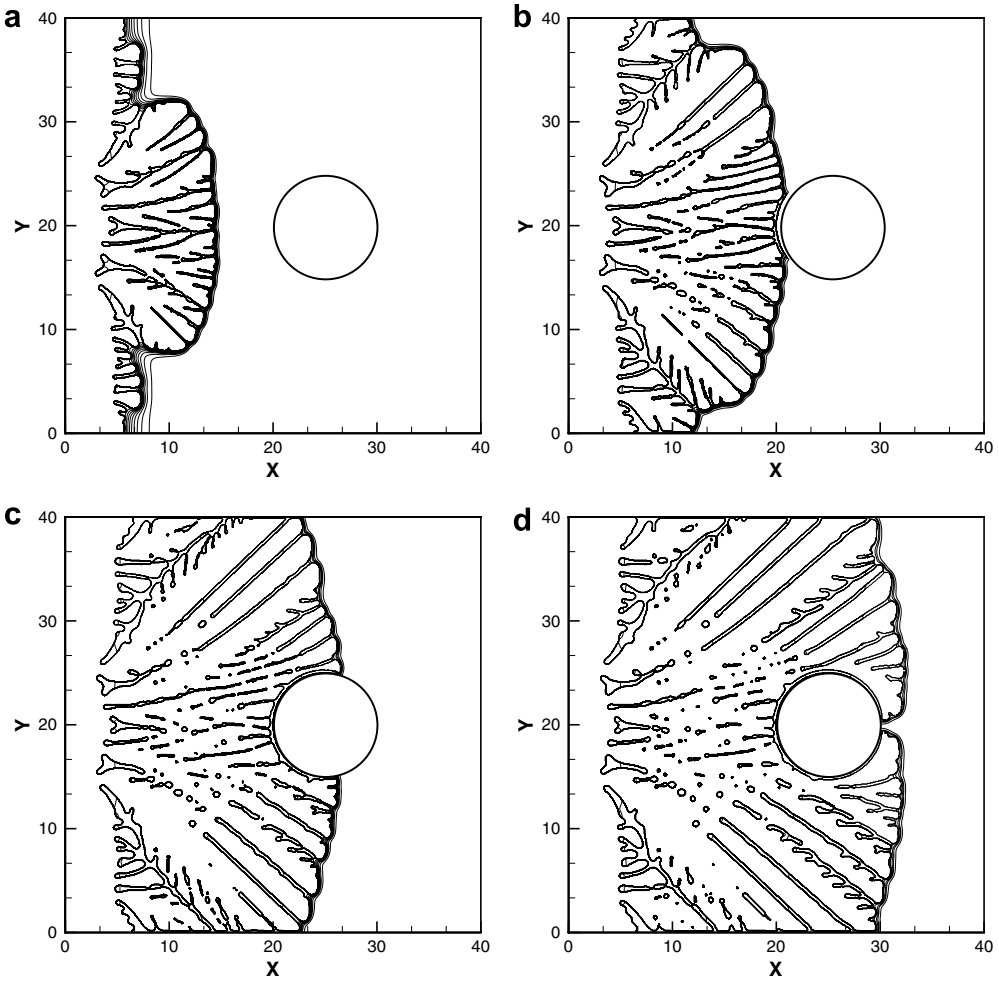


Fig. 13. The species concentration contours (for a front approaching a particle asymmetrically) shown at different times for the directional solidification process in the presence of a ceramic particle ($k_P/k_L = 0.01$). The interface shape and non-dimensional species concentration are shown at four different instants during the development of the instability.

gradient in front of the moving solidification front, the effect of different particle melt thermal conductivity ratio is not *a priori* obvious. Therefore, simulations of the solidification front approach to the particle were carried out by varying the particle thermal conductivity. It is observed that the behaviors of the growing cells are very much the same for different particle melt thermal conductivity ratios. Fig. 10 shows that for a particle melt thermal conductivity ratio $k_P/k_L = 1$, the evolution of the profile of the growing cell. Practically no differences are seen between Figs. 9 and 10. In each case, as the cellular structure goes around the particle liquid pools remain between the particle and the front. The cells all grow around the particle and finally engulf it. For a case of thermal conductivity ratio of $k_P/k_L = 10$, the simulation results essentially reproduce the scenario described above.

Fig. 11 shows the evolution of the growing cell when interacting with a solid particle in front it. The only difference between this case and the case shown in Fig. 9 is that the perturbation wave number used in this case corresponds to a low growth rate perturbation wave number, while the cases shown in Figs. 9 and 10 use a perturbation wave number corresponding to high growth rate perturbation wave-number [14]. The result shown in Fig. 11 indicates that the presence of the particle can have a significant impact on the stability of the interface. Due to the low growth rate, the solidification front initially grows as a slightly perturbed interface until it reaches the vicinity of the particle region. As the particle is approached the obstruction of the species diffusion by the particle is felt by the solidification front, and the growth of solidification front right beneath the particle is suppressed. The sides far from the particle continue to grow and the cellular growth of the interface away from the particle is actually enhanced. The final profile takes a shape as shown in Fig. 11d before the growing interface approaches the boundary of the fine mesh region.

Fig. 12 shows that when the particle is placed in front of the interface asymmetrically with respect to the growing cell, the cell grows around the particle along one side (with the same high growth perturbation wave-number here in this case as in the case shown in Fig. 9). The growth of

the side that is directly under the particle is suppressed and the cell grows towards the other side where the species diffusion path is not blocked as much. Thus, the presence of a particle has the overall effect of suppressing instability growth in its vicinity in a binary alloy undergoing directional solidification.

Fig. 13 shows the interactions between fully developed cells and the solid particle. In the simulation shown in Fig. 13 the initial perturbation was localized at the center of the solid–liquid interface. Fig. 13a shows that the initial perturbation has grown into cells and the cells spread from the center of the domain (where the original perturbation was placed) to the sides of the domain in trying to occupy more of the available space. Fig. 13b depicts the stage at which the cells have made contact with the particle. The tips of the cells that reached the particle stop progressing due to the formation of a layer of solute trapped between the cells and the particle, while the other cell tips continue to grow around the particle. Fig. 13c and d shows that the particle is finally engulfed by the cells. The present sharp interface method captures not only the interaction of the cells with the particle but also the evolution of the myriad pockets of solute that are left behind and retained in the mushy region as the cellular front grows.

In all of the above cases the particle was maintained stationary while the interface progressed around it. For the computed cases the gap between the cells and the particle are significant enough that interaction between the front and the particle that may lead to particle pushing effects are not likely, since the particle pushing mechanism starts to act only at a much smaller length scale. In all cases it can be surmised that the particle will either be engulfed by the interface or entrapped between side-arms. A large part of the literature on particle–front interactions has focused on the pushing to engulfment transition and the determination of the critical velocity for this transition. These studies are mainly concerned with stable planar interfaces approaching particles. In the present study, for the unstable fronts, whether dendritic or cellular, it appears that the particle will be engulfed or entrapped by the dendritic sidebranches and cellular structures. Therefore, conclusions drawn from planar front–particle interaction studies do not apply in the present situation.

## 4. Conclusion

A sharp interface level-set based numerical method is applied to simulate the directional solidification of binary alloys in the presence of the particle. The transport of solute and heat are computed. The directional solidification calculations are first validated against the Mullins–Sekerka stability theory and the stability spectrum is reproduced by the computations. The interaction of the cellular interface with a ceramic particle in the melt is then computed. It is shown that, in contrast to the case of a pure material, the ratio of thermal conductivity of the particle to the melt plays no role in determining the front morphology and the result of the particle–front interaction. The diffusion of species controls the evolution of the phase front around the particle. The particle appears to suppress the instability of the front in its vicinity. This is because of the hindrance that it presents to solute diffusion. In each of the computed cases the front avoids the particle and travels around it in the direction of the steepest solute gradient (i.e. independent of the thermal gradient). There is always a significant thickness of liquid present between the front and the particle as the front engulfs the particle. Therefore, it is difficult to envision a pushing-type interaction between the front and the particle in binary alloy directional solidification.

## Acknowledgements

This work was supported by a National Science Foundation CAREER Award (CTS-0092750) to the third author. Helpful discussion with Professor Christoph Beckermann and Post-Doctoral researcher (U Iowa), Dr. Arnoldo A. Badillo, was highly appreciated.

## References

[1] R. Asthana, S.N. Tewari, Review the engulfment of foreign particles by a freezing interface, J. Mater. Sci. 28 (1993) 5414–5425.
[2] J. Pötschke, V. Rogge, On the behaviour of foreign particles at an advancing solid liquid interface, J. Cryst. Growth 94 (1989) 726–738.
[3] D.K. Shangguan, S. Ahuja, D.M. Stefanescu, An analytical model for the interaction between an insoluble particle and an advancing solid/liquid interface, Metall. Mater. Trans. A 23 (A) (1992) 669–680.
[4] Y. Yang, J.W. Garvin, H.S. Udaykumar, Sharp interface simulation of interaction of a growing dendrite with a stationary solid particle, Int. J. Heat Mass Transfer 48 (2005) 5270–5283.
[5] G. Wilde, J.H. Perepezko, Experimental study of particle incorporation during dendritic solidification, Mater. Sci. Eng. A 283 (1–2) (2000) 25–37.
[6] J.W. Garvin, H.S. Udaykumar, Particle-solidification front dynamics using a fully coupled approach: Part I. Methodology, J. Cryst. Growth 252 (1–3) (2003) 451–466.
[7] J.W. Garvin, H.S. Udaykumar, Particle-solidification front dynamics using a fully coupled approach: Part II. Comparison of drag expressions, J. Cryst. Growth 252 (1–3) (2003) 467–479.
[8] J.S. Langer, Recent developments in the theory of pattern formation, Physica A 140 (1–2) (1986) 44–50.
[9] D.A. Kessler, H. Levine, Pattern selection in three dimensional dendritic growth, Acta Metall. 36 (10) (1988) 2693–2706.
[10] W.W. Mullins, R.F. Sekerka, Stability of a planar interface during solidification of a dilute binary alloy, J. Appl. Phys. 35 (2) (1964) 444–451.
[11] R.A. Brown, H.K. Do, Modeling of directional solidification from scheil to detailed numerical simulation, J. Cryst. Growth 109 (1–4) (1991) 50–65.
[12] W.J. Boettinger, J.A. Warren, Simulation of the cell to plane front transition during directional solidification at high velocity, J. Cryst. Growth 200 (3–4) (1999) 583–591.
[13] C.W. Lan, Quantitative phase field simulation of deep cells in directional solidification of an alloy, Acta Mater. 53 (8) (2005) 2285–2294.
[14] B. Echebarria, R. Folch, A. Karma, M. Plapp, Quantitative phase-field model of alloy solidification, Phys. Rev. E 70 (6) (2004), 061604.1-22.
[15] J.J. Derby, R.A. Brown, On the dynamics of Czochralski crystal growth, J. Cryst. Growth 83 (1) (1987) 137–151.

[16] J.J. Derby, R.A. Brown, On the quasi-steady-state assumption in modeling, Czochralski crystal growth, J. Cryst. Growth 87 (2–3) (1988) 251–260.
[17] Y. Yang, H.S. Udaykumar, Sharp interface Cartesian grid method III: solidification of pure materials and binary solutions, J. Comput. Phys. 210 (1) (2005) 55–74.
[18] H.S. Udaykumar, L. Mao, R. Mittal, A finite-volume sharp interface scheme for dendritic growth simulations: comparison with microscopic solvability theory, Numer. Heat Transfer B 42 (5) (2002) 389–409.
[19] P. Zhao, M. Venere, J.C. Heinrich, D.R. Poirier, Modeling dendritic growth of a binary alloy, J. Comput. Phys. 118 (2003) 434–461.
[20] C.Y. Li, S.V. Garimella, J.E. Simpson, Fixed grid front-tracking algorithm for solidification problem: Part II. Directional solidification with melt convection, Numer. Heat Transfer B 43 (2) (2003) 143–166.
[21] J.A. Sethian, Level Set Methods and Fast Marching Methods, second ed., Cambridge University Press, Cambridge, 1999.
[22] R. Trivedi, Pattern formation during the directional solidification of binary systems, Acta Metall. 33 (6) (1985) 1061–1068.
[23] R. Trivedi, S. Liu, B. Echebarria, A. Karma, Cellular pattern selection in directional solidification, JOM 56 (11) (2004) 19.
[24] W. Kurz, D.J. Fisher, Fundamentals of Solidification, fourth ed., Trans-Tech Publications, Switzerland, 1998.
[25] M. Georgelin, A. Pocheau, Onset of side branching in directional solidification, Phys. Rev. E 57 (3) (1998) 3189–3203.